Thermal conductivity of amorphous NbO_x thin-films and its effect on volatile memristive switching

Sanjoy Kumar Nandi[a], Sujan Kumar Das[a,b], Yubo Cui[c], Assaad El Helou[c], Shimul Kanti Nath[a,d], Thomas Ratcliff[a], Peter. Raad[c] and Robert G. Elliman[a]*

[a] Department of Materials Physics, Research School of Physics, Australian National University, Canberra, Australian Capital Territory, 2601, Australia

[b] Department of Physics, Jahangirnagar University, Dhaka,1342, Bangladesh

[c] Mechanical Engineering Department, Southern Methodist University, Dallas, Texas 75275, United States

[d] Department of Electrical, Electronic and Computer Engineering, The University of Western Australia, Crawley, Western Australia, 6009, Australia

E-mail: sanjoy.nandi@anu.edu.au

Abstract

Metal-oxide-metal (MOM) devices based on niobium oxide exhibit threshold switching (or current controlled negative differential resistance) due to thermally-induced conductivity changes produced by Joule heating. A detailed understanding of the device characteristics therefore relies on an understanding of the thermal properties of the niobium oxide film and the MOM device structure. In this study, we use time-domain thermo-reflectance to determine the thermal conductivity of amorphous NbO_x films as a function of film composition and temperature. The thermal conductivity is shown to vary between 0.86 and 1.25 $Wm^{-1}K^{-1}$ over the composition (x= 1.9 to 2.5) and temperature (293 to 453 K) ranges

examined, and to increase with temperature for all compositions. The impact of these thermal conductivity variations on the quasi-static current-voltage (I-V) characteristics and oscillator dynamics of MOM devices is then investigated using a lumped element circuit model. Understanding such effects is essential for engineering functional devices for non-volatile memory and brain-inspired computing applications.

KEYWORDS: Thermal conductivity, memristor, electroforming, volatile memory, negative differential resistance, niobium oxide

Introduction

Two-terminal metal/oxide/metal (MOM) devices based on amorphous NbO_x have attracted research interest in recent years due to the fact that they exhibit reliable threshold switching or current-controlled negative differential resistance (CC-NDR)[1-3]. Of particular interest is their application as selector elements in non-volatile memory arrays and as nanoscale relaxation oscillators, which when coupled can be used to emulate the spiking response of biological neurons for application in high-density neural networks[1, 4] The functionality of such devices is further enhanced by the diversity of their current-voltage characteristics, which include a broad range of discrete and mixed mode behaviour[4].

The CC-NDR characteristics of NbO_x-based devices derive from an increase in the electrical conductivity of the oxide film due to local Joule heating[5-6]. However, heating is confined to a small volume of material within the thin-film layer and therefore depends on the thermal conductivity of the surrounding material[7-8]. This arises from the fact that as-fabricated MOM devices are typically in a high resistance state and require a one-off electroforming step to create a conduction path through the oxide film[8-9]. As an example, Figure 1(a) shows an optical image of a cross-point device after electroforming. The dark spot is due to discoloration of a photoresist layer as a result of local heating and serves to show the scale and spatial location of the filamentary conduction path[8]. Following electroforming, the device current and associated temperature-rise are largely confined to this filamentary conduction path (Figure 1 (c-d)) and the corresponding increase in oxide conductivity is observed as CC-NDR (Figure 1(e))[9].

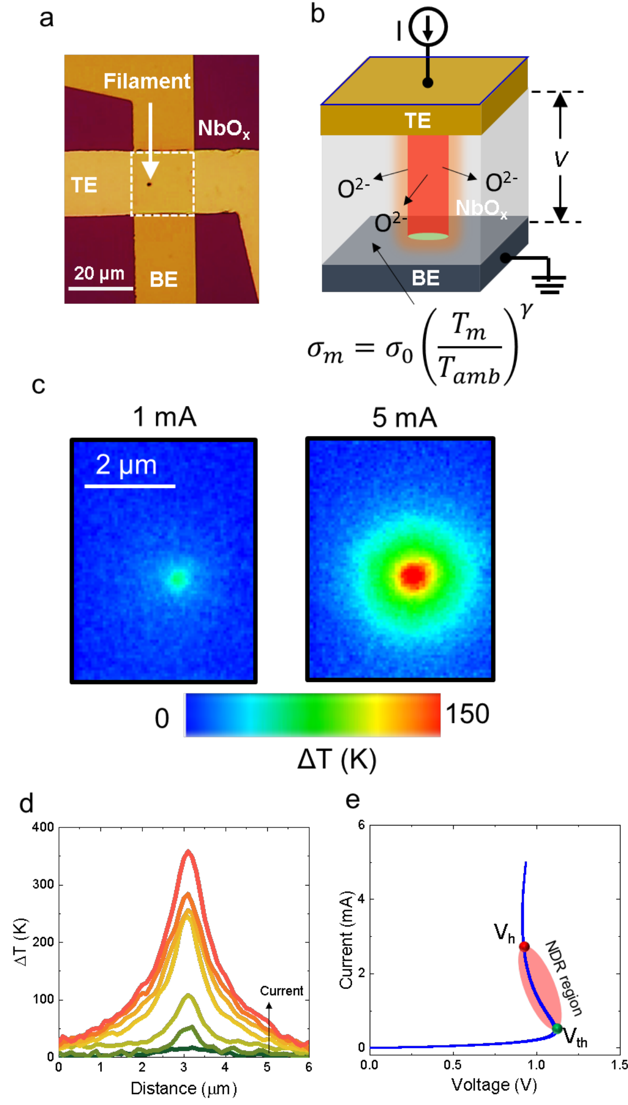

Figure 1: (a) Optical image of an electroformed device showing filament location. (b) Schematic of permanent filament formation due to the Soret effect. (c) Thermoreflectance maps of the surface temperature in a 5 μm device operating at 1 mA and 5 mA and (d) temperature constriction of S-type NDR in the post-formed device at different current levels of the NDR region of the current-voltage characteristics as shown in (e).

From the above discussion, it is clear that the temperature distribution around the filamentary conduction path depends on the thermal conductivity of the oxide film, with significant radial heat flow expected from the filament to the surrounding film and from the film to the electrodes. Knowledge of the thermal conductivity and its temperature

dependence is therefore critical for effective modelling of the temperature distribution and the associated device characteristics.

Thermal transport in low-conductivity crystalline solids is dominated by phonons, and can be described within the framework of a phonon gas model in which the phonons are treated as quasi-particles that travel at their group velocity along straight paths and scatter from impurities, defects, interfaces and other phonons[10]. However, amorphous solids lack the translational symmetry required to define phonons in terms of vibration modes with characteristic wavevectors. Instead, lattice vibrations are considered to be independent and uncorrelated, with heat conduction achieved by a diffusive random-walk process. Recent studies have generalised such analysis by classifying the transport into three regimes: propagons, diffusons, and locons (localized modes), where propagons are phonon-like modes that have well-defined wave vectors and travel multiple atom spacings, diffusons represent the diffusive, random-walk transport, and locons represent highly localised modes[11-14]. Other recent studies have also shown that the thermal conductivity of thin film ($\leq 100\,nm$) amorphous solids is typically dominated by diffusons[14-16], and estimates of the minimum thermal conductivity based on such diffusive transport have been proposed by Cahill *et al*[17] and Agne *et al*[18].

The thermal conductivity of amorphous Nb_2O_5 films has been measured over the temperature range from 293 to 773 K[16, 19]. Cheng et. al[16] used time-domain thermoreflectance (TDTR) to measure the thermal conductivity of Nb_2O_5 films deposited by reactive DC sputtering of a Nb target in an oxygen ambient. They reported a temperature independent thermal conductivity of ~0.9 $Wm^{-1}K^{-1}$ over the temperature range from 325 to 450 K. Mitterhuber *et al*[19] employed two different TDTR systems to measure the thermal conductivity of a 166 nm thick Nb_2O_5 film on silicon, one using a nanosecond pump beam and the other using a picosecond pump. The measured thermal conductivity showed some variation for the two measurements due to

differences in the effective penetration depth of the thermal pulse. In both cases the thermal conductivity was found to increase with temperature, varying from ~1.0 to ~1.25 $Wm^{-1}K^{-1}$ over the temperature range 293 to 573 K as measured by the nanosecond pump, and from 1.0 to 2.25 over the temperature range 293 to 775 K as measured by the picosecond pump.

In this study, we use time-domain thermo-reflectance (TDTR) to determine the thermal conductivity of amorphous NbO_x films as a function of both film composition and temperature for the first time. We further investigate how the magnitude and temperature dependence of the thermal conductivity affect the quasi-static current-voltage characteristics and oscillator dynamics of MOM-based devices. These results are discussed with reference to minimum thermal conductivity models for amorphous solids, and their significance for effective device engineering is demonstrated.

Experimental details

NbO_x dielectric layers of varied composition (x=1.9 to 2.5) and thickness were sputter deposited onto silicon and amorphous carbon substrates. Stoichiometric films (x=2.5) were deposited by RF sputtering using an Nb_2O_5 target and an Ar ambient, while substoichiometric films (i.e. x<2.5) were deposited using reactive DC sputtering of an Nb target in a process ambient of variable O_2/Ar ratio and pressure. Details of the deposition conditions are given in Table 1. The stoichiometry and areal atomic-density of the films was determined by Rutherford backscattering spectrometry (RBS) of films deposited onto vitreous carbon or Si substrates. Data fitting was undertaken with the RUMP software package[20] using corrected stopping power data for Nb[21]. The mass density of the films was determined by combining RBS measurements and layer thicknesses determined from transmission electron microscopy (TEM) of sample cross-sections. The as-deposited films were further analysed using X-ray photoelectron spectroscopy (XPS). The structure of the films was investigated by electron-

diffraction analysis during TEM imaging and by grazing incident-angle X-ray diffraction (GIA-XRD). Finally, the surface morphology and roughness of the films was determined by atomic force microscopy (AFM).

Thermal conductivity measurements were undertaken using time-domain thermoreflectance (TDTR). For these measurements the NbO_x layers were deposited on silicon substrates and then coated with a 130 nm thick gold absorptive/transducer layer using electron beam evaporation. The measurements were performed using a TMX Scientific Transometer™ TDTR, with an Nd:YAG laser of wavelength 532 nm used for the pulse excitation and an Argon-Ion 488 nm CW laser used for probing. The NbO_x samples were placed on a temperature-controlled hotplate (Temptronic ThermoChuck® TP04310) that enabled measurements over the temperature range from 293 K to 453 K. Measurements were repeated 10 times on each sample and averaged. As the dimensions of the pump beam are two orders of magnitude larger than those of the probe beam, the Transometer's analysis uses a one-dimensional thermal transport computational model through the thin-film stack[22, 23].). Electrical characterization (see supplementary information) was performed using a semiconductor parametric analyser (Agilent B1500A).

Table 1: Deposition conditions and properties of NbO_x films

Target	**Ar/O_2 (sccm)**	**Power (W)**	**Pressure (mT)**	**x in NbO_x**	**Dep. Rate (nm/min)**	**Density ($g.cm^{-3}$)**	**Thickness (nm)**
Nb	19/1	100	1.5	1.9 ± 0.1	3.4	5.73	32, 71, 101
Nb	18.5/1.5	100	1.5	2.0 ± 0.1	3.2	5.75	32, 64, 93, 127
Nb	19/1	100	2.0	2.3 ± 0.1	2.6	5.35	25, 49, 76, 103
Nb_2O_5	20/0	180	4.0	2.5 ± 0.1	2.5	4.3	13, 25, 50, 75, 100

Results and discussion

Physical properties of NbO_x thin films

The composition and areal atomic-density (i.e. atoms.cm^{-2}) of the NbO_x films were determined by Rutherford backscattering spectrometry (RBS) using 2 MeV He^+ ions. Figure 2a shows a measured spectrum for a 127 nm thick $NbO_{2.0}$ film, together with a simulated spectrum fitted to the data using the RUMP software package[22] with updated stopping power data for Nb[21]. We have previously studied similar films by Reflection Electron Energy Loss Spectroscopy (RHEELS) and shown that the substoichiometric NbO_x films do not contain metallic Nb[23]. Transmission electron microscopy (TEM) of sample cross-sections was used to further characterize the layer thickness, structure and morphology. Figure 2b shows an example for the 127nm thick $NbO_{2.0}$ film, which highlights the presence of density variations in the amorphous film due to columnar growth. Such type of growth is a characteristic of sputter-deposited films and has been shown to influence the electroforming behaviour of MOM devices[24].

The amorphous structure of the films was confirmed by grazing-incidence x-ray diffraction (GI-XRD), with spectra of the as-deposited NbO_x films displaying only broad peaks indicative of amorphous NbO_x, as shown in Figure 2c. The average film densities were determined from the areal atomic densities, as measured by RBS, and the film thicknesses, as determined from TEM, and were found to be in reasonable agreement with those of Venkataraj *et al*[25]. Atomic force microscopy (AFM) was used to measure the surface roughness of the NbO_x films as a function of film thickness. Results are summarized in Figure 2(d) and show that the root-mean-square (RMS) roughness increases as the film thickness increases. The $NbO_{2.5}$ films have relatively higher roughness than the others, as they were deposited at a higher power and with higher gas pressure[26-27].

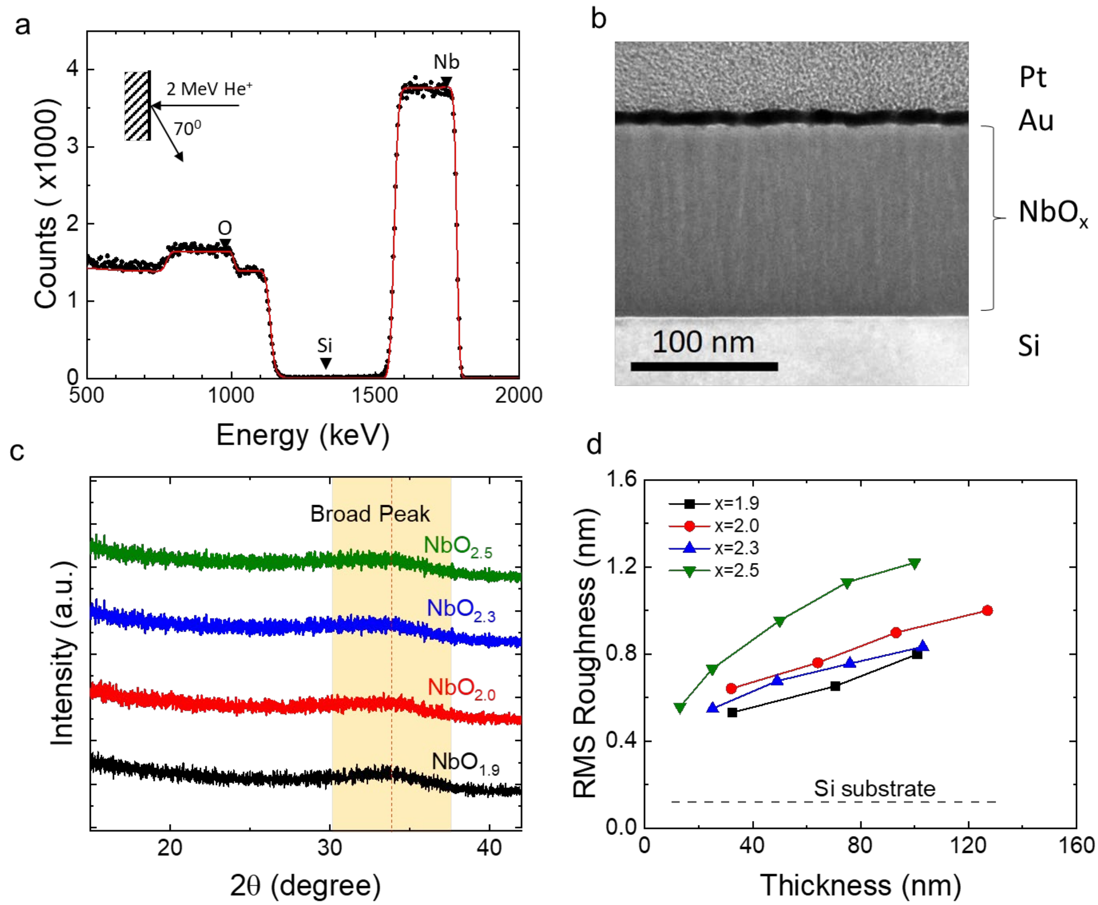

Figure 2: Physical characterisation of films: a) RBS spectrum of a 127nm thick $NbO_{2.0}$ film, together with spectrum simulated using the RUMP software package; b) a bright field TEM image of the same film. (NB: A 10 nm Au layer was used to provide contrast); c) GI-XRD spectra of the thickest films, and; d) RMS roughness of the films as measured by AFM. The dashed line represents the roughness of the Si substrate.

Time domain thermoreflectance

Time-domain thermoreflectance (TDTR) is a pump and probe technique that uses changes in optical reflectivity to measure the temperature evolution of a gold surface layer heated by a short laser pulse, as shown schematically in Figure 3a. The thermal decay on the top metallic surface after the laser pulse is driven by the heat loss from the irradiated area and is therefore sensitive to the thermal diffusivity of the underlying constituent materials[28]. In this study, we

used a thin gold layer as the temperature sensing layer due to its relatively high thermoreflectance coefficient and chemical inertness. The temporal response of the surface temperature was modelled for the resulting film stack using the Fourier equation, with the thermal diffusivity of the NbO_x layer employed as a fitting parameter. Given that the heated area is much larger than the probe area, heat dissipation is assumed to be dominated by through-plane conduction (i.e., the z-direction) from the gold surface layer down to the base of the substrate which is maintained at room temperature. The governing equation is then given by:

$$\rho_{C_P} \frac{\partial \theta}{\partial t} = \frac{\partial}{\partial z}\left(k \frac{\partial \theta}{\partial z}\right) + Q_{ab}(z,t) \qquad (1)$$

where θ is the normalized temperature in the sample stack. The density (ρ) of the NbO_x layers was determined from RBS, TEM and XRR measurements, as discussed above, while the temperature-dependent specific heat, c_p, was calculated from the Shomate equation by extrapolating between data for Nb, NbO, NbO_2 and Nb_2O_5 from the National Institute of Standards and Technology (NIST) (see Supporting information) [29]. Any heat transfer from the top surface (z = 0) by convection or radiation is negligible and the top boundary is thus considered adiabatic ($\partial\theta/\partial z = 0$), while the temperature of the bottom surface of the substrate is considered as the reference base temperature ($\theta = \theta_b$ at $z \rightarrow \infty$). The heat generation term Q_{ab} represents the optical absorption of the laser pulse by the gold layer and is given by:

$$Q_{ab}(z,t) = I(t)(1-R)\gamma e^{-\gamma z} \qquad (2)$$

$$I(t) = \frac{2F}{\tau\sqrt{\pi}} e^{-4\left((t-t_0)/\tau\right)^2} \qquad (3)$$

where, *I(t)*, *F*, and *τ* are the intensity, fluence, and the pulse width of the heating laser; *R* and *γ* are the reflectivity and the absorption coefficient of the gold surface. The absorption coefficient is obtained from the laser wavelength, *λ*, and refractive index, *k*, of the Au absorption layer as $\gamma = 4\pi k/\lambda$. Analytical solutions of Eq. (1) exist for semi-infinite media, but for film stacks,

the equation is most easily solved numerically and fitted to the observed TDTR response using the thermal boundary resistance, R^B_{TDTR}, as a fitting parameter. Figure 3b shows an example of the TDTR response for NbO_x films as a function of thickness, together with the fitted 1-D numerical solutions of Eq. (1).

Based on a thermal circuit model of the thin-film structure[23], the total thermal boundary resistance is given by:

$$R^B_{TDTR} = \frac{h}{k_i} + R_{int} \tag{4}$$

where h is the film thickness, k_i is the intrinsic thermal conductivity of the NbO_x film and R_{int} represents the thermal interface resistance that includes contributions from the Au/NbO_x and NbO_x/Si interfaces. The intrinsic thermal conductivity and interface resistance can therefore be deduced from a plot of R^B_{TDTR} as a function of film thickness, such as that shown in Figure 3c for the $NbO_{2.0}$ films. This data clearly demonstrates the expected linear relationship between R^B_{TDTR} and film thickness and provides the magnitude of the thermal interface resistance (i.e., the intercept). The latter was found to vary from 37 to 51 m^2K/GW with film composition, but to have only a weak temperature dependence, as shown in Figure 3c.

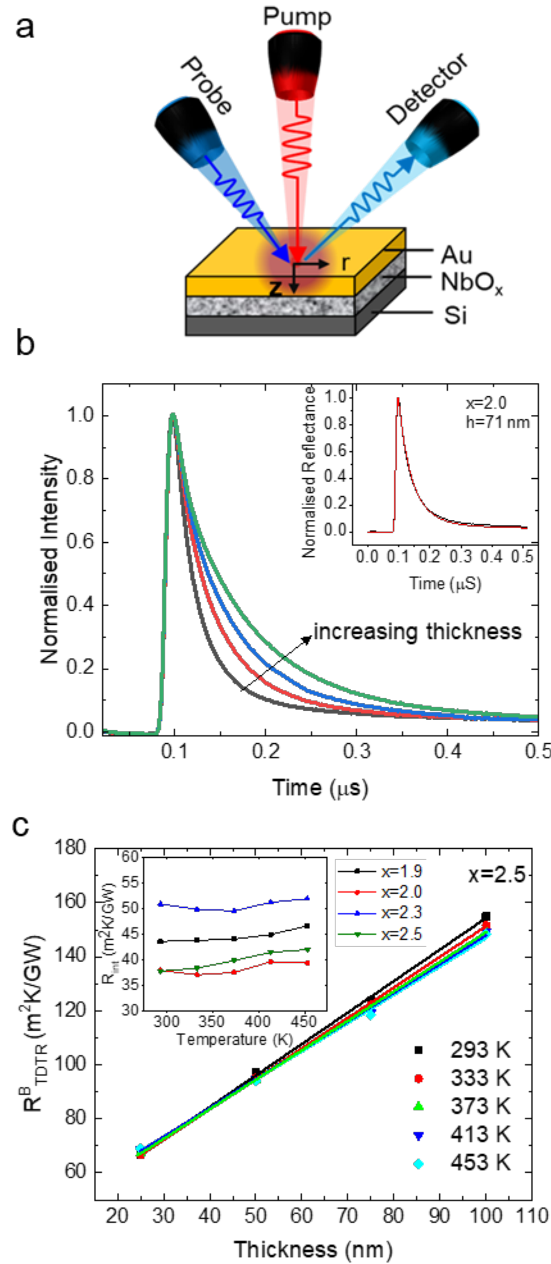

Figure 3: a) Schematic representation of the Pump-Probe setup used to conduct transient-domain thermo-reflectance conductivity measurements; b) Normalized TDTR response showing the temperature decay measured at the surface of the gold transducer layer for an $NbO_{2.0}$ film as a function of thickness. The inset shows the measured response for a 71-nm film together with the fitted response, and c) R^{B}_{TDTR} as a function of layer thickness and temperature for the $NbO_{2.5}$ films. The inset shows the interface resistance, R_{int}, for all films as a function of temperature.

Thermal conductivity of NbO$_x$ layers

The thermal conductivity values extracted from the above analysis are shown in **Figure** 4(a) for NbO$_x$ layers with x in the range from 1.9 to 2.5 and temperatures in the range from 293 to 473 K. Several points are evident from this data. First, the magnitude of the thermal conductivity varies between extremes of 0.86 and 1.25 $Wm^{-1}K^{-1}$ over the composition and temperature range examined, which is broadly consistent with values reported for other amorphous oxide films[14, 30]. Second, the thermal conductivity increases with temperature for all compositions, with that of the NbO$_{2.5}$ film increasing by 11%, from 0.86 to 0.95 $Wm^{-1}K^{-1}$ over the 180 K temperature span. Finally, while the data for different compositions falls broadly within the margin of error, estimated to be ±12%, it suggests that the thermal conductivity of the near-stoichiometric NbO$_{2.0}$ and NbO$_{2.5}$ (i.e., Nb$_2$O$_5$) films is lower than that of the off-stoichiometric NbO$_{1.9}$ and NbO$_{2.3}$ films. The former ranges from 0.85 to 0.95 Wm^{-1}K^{-1}, while that of the NbO$_{1.9}$ and NbO$_{2.3}$ films varies from 1.03 to 1.24 Wm^{-1}K^{-1} over the temperature range from 298 to 453 K. Such behaviour could result from variations in the macroscopic structure of the films, such as porosity or roughness, or from variations in the film microstructure, such as the distribution and site-sharing of NbO$_6$, NbO$_7$ and NbO$_8$ structural units. Unfortunately, the current data are insufficient to draw a definitive conclusion on this issue, but the results do serve to highlight the need for a more detailed study of such effects.

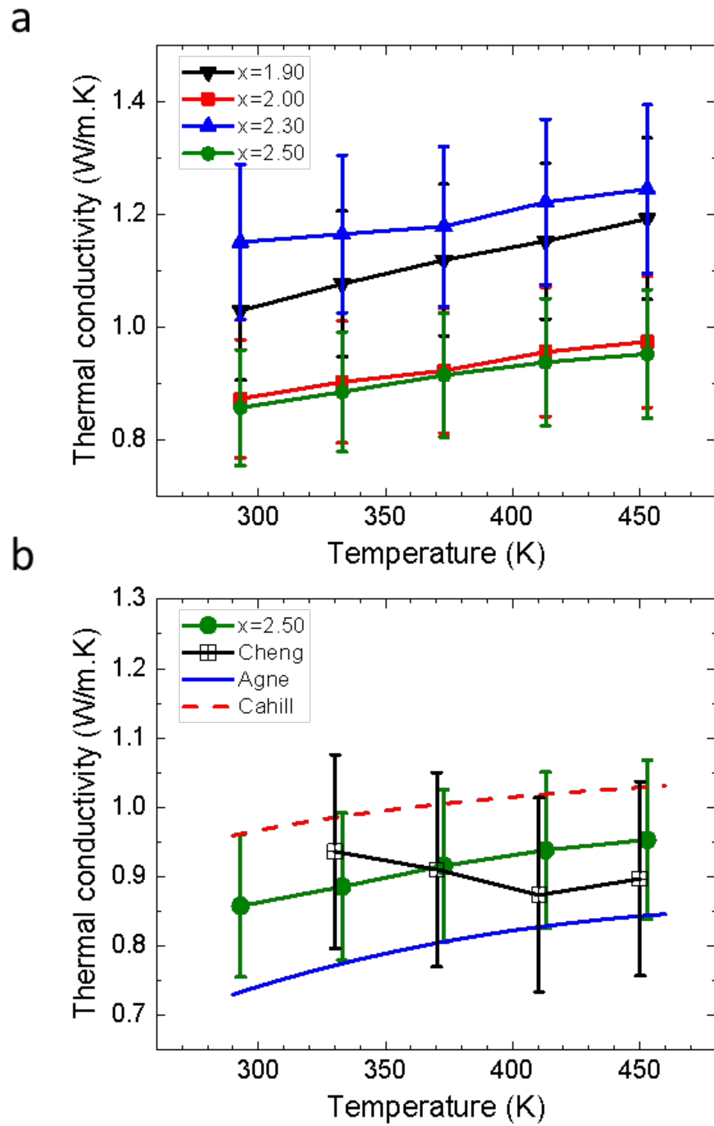

Figure 4: (a) Measured thermal conductivity as a function of stoichiometry and temperature, and (b) Measured thermal conductivity of $NbO_{2.5}$ as a function of temperature compared with the measurements of Cheng *et al*[16] and theoretical predictions of the minimum thermal conductivity expected for amorphous Nb_2O_5 from Cahill *et al*[17] and Agne *et al*[18]. The relative error of repeat measurements was estimated to be ≤±5%, while the absolute error was estimated to be ±12%.

Figure 4(b) compares the temperature dependence of the thermal conductivity measured for the $NbO_{2.5}$ films with the data of Cheng *et al*[16], and with predictions of the minimum thermal conductivity models by Cahill *et al*[17] and Agne *et al*[18]. (Details of the model parameters are given in the Supporting Information). The experimental data are observed to be in excellent agreement and broadly consistent with model predictions. Significantly, the temperature dependence of the thermal conductivity is similar to that predicted by the models for lattice conductivity. Behaviour that supports the view that the thermal conductivity is dominated by the lattice contribution in this temperature range. From the Wiedemann-Franz law, the electronic contribution to the thermal conductivity is $k_{el} = LT\sigma$, where L is the Lorentz number ($2.44 \times 10^{-8}\ W\Omega K^{-2}$), T is the temperature and σ is the electrical conductivity. An electrical conductivity of $\approx 1.5 \times 10^{4}\ Sm^{-1}$ is therefore required to contribute 10% of the measured thermal conductivity (i.e. $\approx 0.1\ Wm^{-1}K^{-1}$). This is much higher than the conductivity of the present films. For example, we have previously measured the electrical conductivity of a $NbO_{2.10}$ film to be $\sigma = 119 + 7.2 \times 10^{5}\exp(-\frac{0.34\ [eV]}{kT})$, which is $< 250\ Sm^{-1}$ over the temperature range of the current measurements. In this case, the electronic contribution to the thermal conductivity is < 0.3% but would rise to ~30% at a temperature of 1000 K. This contrasts with the reported case of sub-stoichiometric TaO_x films, where the electronic contribution is dominant over a wide composition range due to the high electrical conductivity of the films[31].

Implications for device characteristics

As discussed in the introduction, the CC-NDR response of MOM devices results from thermally-induced conductivity changes. The specific I-V response is therefore sensitive to both the magnitude and temperature dependence of the thermal conductivity of the film. Here

we consider the effect of such variations on the quasi-static response and oscillation dynamics of NbO_x-based devices.

The device characteristics were simulated using a lumped-element circuit-model of the volatile memristor developed by Slesazeck *et al*[6]. This model assumes Poole-Frenkel conduction and estimates the local temperature from Joule heating, with the material properties represented by a thermal resistance, R_{th}, and a thermal capacitance, C_{th}. The basic circuit model is shown inset in Figure 5b, and further details and associated parameters are included in the Supporting Information. Variations in thermal conductivity were included in the model by changing R_{th}, which is assumed to have the form:

$$R_{th} = R_{th0}/[1 + \alpha(T - T_{amb})] \quad (5)$$

where R_{th0} was taken to be 1.7×10^5 K/W for x=2.5 based on the model of Slesazeck *et al*[6], and was varied by 30%, from 1.7×10^5 K/W to 1.3×10^5 to reflect the observed variation of the thermal conductivity with stoichiometry. The value of α was set to 0 or 6×10^{-4} K^{-1} to represent temperature-independent and temperature-dependent thermal conductivities, respectively, where the latter represents a ~10% increase in the thermal conductivity between 290 K and 450 K, and a ~43% increase between 290 K and 1000 K.

Figure 5a summarises the effect of thermal conductivity variations on the I-V characteristics of a MOM device. The data show that an increase (decrease) in the magnitude of the thermal conductivity (thermal resistance) shifts the characteristics to higher voltages and reduces the magnitude of the NDR (i.e. the slope of the I-V characteristic). Comparison with the data in Figure 5b shows that this is a direct consequence of a reduction in the device temperature. The lower operating temperature has the effect of increasing the device resistance for a given input current due to the strong temperature dependence of Poole-Frenkel conduction. The reduction in the magnitude of the NDR follows from the fact that the temperature change for a given

incremental increase in current is reduced by an increased thermal conductivity. These predictions are consistent with the experimental observations of Wang *et al.*[32], who studied the effect of thermal resistance on the electrical characteristics of devices by fabricating similar devices of SiO_2/Si substrates and suspended Si_3N_4 membranes. As predicted above, the higher thermal resistance of the suspended devices produced a reduction in the threshold voltage and an increase in the magnitude of the NDR. These results are consistent with the results of the finite element analysis (see supplementary information).

More surprising is the effect of the temperature-dependent thermal conductivity, as this reduces the magnitude of the NDR by around 50%, even though the change in the magnitude of the thermal conductivity with temperature (~25%) is less than the range explored for the temperature independent case (~30%). Such behaviour is particularly significant for engineering memristor-based oscillators because the oscillator dynamics are sensitive to both the magnitude of the NDR and the shape of the differential resistance characteristic.

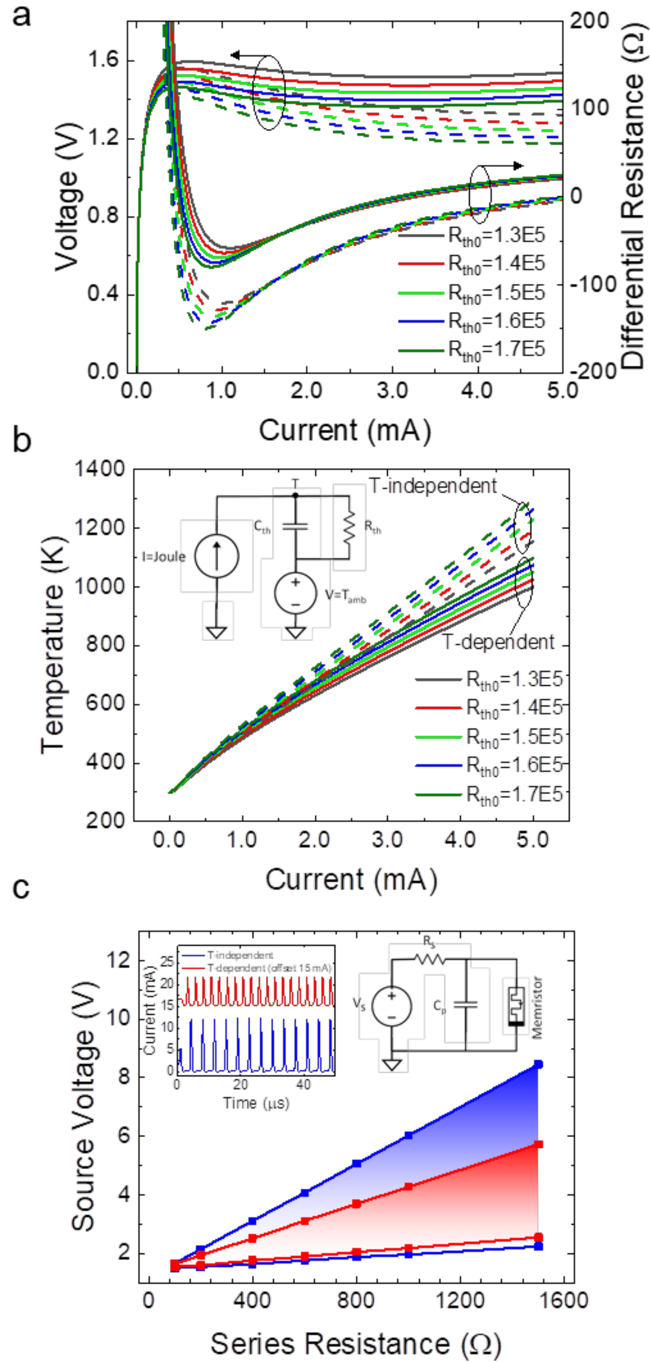

Figure 5: a) Quasi-static I-V characteristics and differential resistance, and b) the temperature of the memristor under current-controlled testing. The inset in b) shows the lumped-element circuit model of the memristor. Dashed lines are for a temperature independent $\mathrm{R_{th}}$ ($\alpha = 0\ \mathrm{K^{-1}}$) and solid lines are for a temperature dependent $\mathrm{R_{th}}$ ($\alpha = 6 \times 10^{-4}\ \mathrm{K^{-1}}$). c) Oscillation dynamics (circuit shown inset) showing $\mathrm{V_s}$-$\mathrm{R_s}$ oscillation window for temperature-independent (blue) and temperature-dependent (red) $\mathrm{R_{th}}$ ($\mathrm{R_{th0}} = 1.7 \times 10^{5}$ K/W). Also shown inset are the

oscillator responses for temperature independent (blue) and temperature dependent (red) R_{th} (V_s=3.0 V, R_s=1 kΩ, $C_p = 10pF$, $R_{th0} = 1.7 \times 10^5$ K/W).

As an example, Figure 5c compares the characteristics of oscillators (see inset) comprised of memristors with temperature-independent and temperature-dependent thermal conductivities. The oscillation window (i.e. The V_s-R_s range for which stable oscillation is observed) is found to be significantly reduced for latter cases, which is a direct consequence of the change in characteristics shown in Figure 5a. The oscillator dynamics for given operating conditions are also impacted by including the temperature-dependent conductivity, as shown in the inset. This compares the memristor current for the two cases under the conditions where V_s=3.0 V, R_s=1 kΩ, $C_p = 10pF$ and $R_{th0} = 1.7 \times 10^5$ K/W Including the temperature dependence is shown to increase the oscillator frequency from 270 kHz to 400 kHz and to reduce the peak amplitude from 12 mA to 6 mA, reflecting the reduction in the magnitude of the NDR. Clearly, these are significant effects that must be accounted for during device engineering.

Conclusions

The thermal conductivity of NbO_x films was measured as a function of stoichiometry, for x in the range from 1.9 to 2.5, and for temperatures in the range from 290 to 453 K, parameter ranges over which NbO_x-based MOM devices exhibit volatile threshold switching and current-controlled negative differential resistance[7, 33]. The magnitude of the thermal conductivity was shown to vary between 0.86 and 1.25 $Wm^{-1}K^{-1}$ over the composition and temperature range examined, and to increase with temperature for all compositions. While the values for films of different composition were broadly within experimental error, the thermal conductivity of near-stoichiometric $NbO_{2.0}$ and $NbO_{2.5}$ (i.e., Nb_2O_5) films was generally lower than that that of off-stoichiometric $NbO_{1.9}$ and $NbO_{2.3}$ films. However, the significance of this observation and the role of film macrostructure and microstructure remain to be confirmed. The thermal

conductivity of all films was shown to increase with temperature and to have a dependence consistent with that of the minimum thermal conductivity models of Cahill *et al*[17] and Agne *et al*[18]. Based on this behaviour and estimates of the electrical conductivity, it was concluded that the thermal conductivity of the NbO_x is dominated by the lattice contribution.

Variations in the thermal conductivity of NbO_x were shown to modify the quasi-static I-V characteristics and oscillator dynamics of NbO_x-based memristive devices, with the temperature dependence of the thermal conductivity playing a particularly significant role. Most notably, the inclusion of the temperature dependence was shown to restrict the voltage-resistance operational window of a simple oscillator, and to affect the frequency and amplitude of the oscillator current. Such behaviour highlights the importance of understanding the thermal properties of devices and the potential of thermal-engineering for tuning the NDR characteristics NbO_x-based memristors.

Acknowledgments

This work was partly funded by the Australian Research Council (ARC) and Varian Semiconductor Equipment/Applied Materials through an ARC Linkage Project Grant: LP150100693. We would like to acknowledge access to NCRIS facilities at the ACT node of the Australian National Fabrication Facility (ANFF) and the Australian Facility for Advanced ion-implantation Research (AFAiiR), a node of the Heavy-Ion Accelerator Capability. Shimul Kanti Nath acknowledges the support of the Forrest Prospect Fellowship awarded by the Forrest Research Foundation, Australia. We also acknowledge the facilities and the scientific and technical assistance of the Australian Microscopy & Microanalysis Research Facility at the Centre of Advanced Microscopy, The Australian National University.

AUTHOR INFORMATION

Corresponding Author

*E-mail: sanjoy.nandi@anu.edu.au (S. K. Nandi)

Supporting Information

Calculation of minimum thermal conductivity and lumped element modelling of negative differential resistance are described. Further, the lumped element model of threshold switching with finite element modelling results are presented. This material is available free of charge via the Internet at http://pubs.acs.org.

References

1. Pickett, M. D.; Medeiros-Ribeiro, G.; Williams, R. S., A Scalable Neuristor Built with Mott Memristors. *Nat. Mater.* **2013,** *12* (2), 114.

2. Nandi, S. K.; Li, S.; Liu, X.; Elliman, R. G., Temperature Dependent Frequency Tuning of Nbox Relaxation Oscillators. *Applied Physics Letters* **2017,** *111* (20), 202901.

3. Li, S.; Liu, X.; Nandi, S. K.; Venkatachalam, D. K.; Elliman, R. G., High-Endurance Megahertz Electrical Self-Oscillation in Ti/Nbox Bilayer Structures. *Appl. Phys. Lett.* **2015,** *106* (21), 212902.

4. Kumar, S.; Strachan, J. P.; Williams, R. S., Chaotic Dynamics in Nanoscale Nbo2 Mott Memristors for Analogue Computing. *Nature* **2017,** *548* (7667), 318.

5. Gibson, G. A., Designing Negative Differential Resistance Devices Based on Self-Heating. *Advanced Functional Materials* **2018,** *28* (22), 1704175.

6. Slesazeck, S.; Mähne, H.; Wylezich, H.; Wachowiak, A.; Radhakrishnan, J.; Ascoli, A.; Tetzlaff, R.; Mikolajick, T., Physical Model of Threshold Switching in Nbo 2 Based Memristors. *RSC Adv.* **2015,** *5* (124), 102318-22.

7. Nandi, S. K.; Nath, S. K.; El-Helou, A. E.; Li, S.; Liu, X.; Raad, P. E.; Elliman, R. G., Current Localization and Redistribution as the Basis of Discontinuous Current Controlled Negative Differential Resistance in Nbox. *Adv. Funct. Mater.* **2019,** *29* (50), 1906731.

8. Nath, S. K.; Nandi, S. K.; Li, S.; Elliman, R. G., Detection and Spatial Mapping of Conductive Filaments in Metal/Oxide/Metal Cross-Point Devices Using a Thin Photoresist Layer. *Appl. Phys. Lett.* **2019,** *114* (6), 062901.

9. Nandi, S. K.; Nath, S. K.; El-Helou, A. E.; Li, S.; Ratcliff, T.; Uenuma, M.; Raad, P. E.; Elliman, R. G., Electric Field- and Current-Induced Electroforming Modes in Nbox. *ACS Appl. Mater. Interfaces* **2020,** *12*, 8422−28.

10. Cahill, D. G.; Braun, P. V.; Chen, G.; Clarke, D. R.; Fan, S.; Goodson, K. E.; Keblinski, P.; King, W. P.; Mahan, G. D.; Majumdar, A.; Maris, H. J.; Phillpot, S. R.; Pop, E.; Shi, L., Nanoscale Thermal Transport. Ii. 2003-2012. *Appl. Phys. Rev.* **2014,** *1* (1), 011305.

11. Allen, P. B.; Feldman, J. L.; Fabian, J.; Wooten, F., Diffusons, Locons and Propagons: Character of Atomie Yibrations in Amorphous Si. *Philos Mag B* **1999,** *79* (11-12), 1715-31.

12. DeAngelis, F.; Muraleedharan, M. G.; Moon, J.; Seyf, H. R.; Minnich, A. J.; McGaughey, A. J. H.; Henry, A., Thermal Transport in Disordered Materials. *Nanoscale Microscale Thermophys. Eng.* **2019,** *23* (2), 81-116.

13. Hanus, R.; Gurunathan, R.; Lindsay, L.; Agne, M. T.; Shi, J.; Graham, S.; Jeffrey Snyder, G., Thermal Transport in Defective and Disordered Materials. *Appl. Phys. Rev.* **2021,** *8* (3), 031311.

14. Wingert, M. C.; Zheng, J.; Kwon, S.; Chen, R., Thermal Transport in Amorphous Materials: A Review. *Semicond Sci Technol* **2016,** *31* (11), 113003.

15. Braun, J. L.; Baker, C. H.; Giri, A.; Elahi, M.; Artyushkova, K.; Beechem, T. E.; Norris, P. M.; Leseman, Z. C.; Gaskins, J. T.; Hopkins, P. E., Size Effects on the Thermal Conductivity of Amorphous Silicon Thin Films. *Physical Review B* **2016,** *93* (14).

16. Cheng, Z.; Weidenbach, A.; Feng, T.; Tellekamp, M. B.; Howard, S.; Wahila, M. J.; Zivasatienraj, B.; Foley, B.; Pantelides, S. T.; Piper, L. F. J.; Doolittle, W.; Graham, S., Diffuson-Driven Ultralow Thermal Conductivity in Amorphous Nb2o5 Thin Films. *Physical Review Materials* **2019,** *3* (2), 025002.

17. Cahill, D. G.; Watson, S. K.; Pohl, R. O., Lower Limit to the Thermal Conductivity of Disordered Crystals. *Phys Rev B Condens Matter* **1992,** *46* (10), 6131-40.

18. Agne, M. T.; Hanus, R.; Snyder, G. J., Minimum Thermal Conductivity in the Context of Diffuson-Mediated Thermal Transport. *Energy & Environmental Science* **2018,** *11* (3), 609-16.

19. Mitterhuber, L.; Kraker, E.; Defregger, S., Structure Function Analysis of Temperature-Dependent Thermal Properties of Nm-Thin Nb2o5. *Energies* **2019,** *12* (4).

20. Doolittle, L. R., A Semiautomatic Algorithm for Rutherford Backscattering Analysis. *Nucl Instrum Methods Phys Res Sect B* **1986,** *15* (1-6), 227-31.

21. Moro, M. V.; Bauer, P.; Primetzhofer, D., Experimental Electronic Stopping Cross Section of Transition Metals for Light Ions: Systematics around the Stopping Maximum. *Phys. Rev. A* **2020,** *102* (2), 022808.

22. Climent-Font, A.; Wätjen, U.; Bax, H., Quantitative Rbs Analysis Using Rump. On the Accuracy of the He Stopping in Si. *Nuclear Instruments and Methods in Physics Research Section B: Beam Interactions with Materials and Atoms* **1992,** *71* (1), 81-86.

23. Vos, M.; Liu, X.; Grande, P.; Nandi, S.; Venkatachalam, D.; Elliman, R., The Use of Electron Rutherford Backscattering to Characterize Novel Electronic Materials as Illustrated by a Case Study of Sputter-Deposited Nbox Films. *Nucl. Instrum. Methods Phys. Res., Sect. B* **2014,** *340*, 58-62.

24. Kenyon, A. J.; Singh Munde, M.; Ng, W. H.; Buckwell, M.; Joksas, D.; Mehonic, A., The Interplay between Structure and Function in Redox-Based Resistance Switching. *Faraday Discuss.* **2019,** *213*, 151-63.

25. Venkataraj, S.; Drese, R.; Kappertz, O.; Jayavel, R.; Wuttig, M., Characterization of Niobium Oxide Films Prepared by Reactive Dc Magnetron Sputtering. *physica status solidi (a)* **2001,** *188* (3), 1047-58.

26. Mwema, F.; Akinlabi, E.; Oladijo, O.; Krishna, S., Microstructure and Scratch Analysis of Aluminium Thin Films Sputtered at Varying Rf Power on Stainless Steel Substrates. *Cogent Engineering* **2020,** *7* (1), 1765687.

27. Ling, L.; Tao, X.; Zhongxiao, S.; Chunliang, L.; Fei, M., Effect of Sputtering Pressure on Surface Roughness, Oxygen Vacancy and Electrical Properties of a-Igzo Thin Films. *Rare Metal Materials and Engineering* **2016,** *45* (8), 1992-96.

28. Komarov, P. L.; Raad, P. E., Performance Analysis of the Transient Thermo-Reflectance Method for Measuring the Thermal Conductivity of Single Layer Materials. *International journal of heat and mass transfer* **2004,** *47* (14-16), 3233-44.

29. Chase, M. W. J., Nist-Janaf Themochemical Tables, Fourth Edition. *J. Phys. Chem. Ref. Data* **1998,** *Monograph 9*, 1-1951.

30. Lee, S. M.; Cahill, D. G.; Allen, T. H., Thermal Conductivity of Sputtered Oxide Films. *Physical Review B* **1995,** *52* (1), 253-57.

31. Landon, C. D.; Wilke, R. H. T.; Brumbach, M. T.; Brennecka, G. L.; Blea-Kirby, M.; Ihlefeld, J. F.; Marinella, M. J.; Beechem, T. E., Thermal Transport in Tantalum Oxide Films for Memristive Applications. *Appl Phys Lett* **2015,** *107* (2).

32. Wang, Z.; Kumar, S.; Wong, H. S. P.; Nishi, Y., Effect of Thermal Insulation on the Electrical Characteristics of Nbox Threshold Switches. *Appl Phys Lett* **2018,** *112* (7), 1-6.

33. Kumar, S.; Williams, R. S.; Wang, Z., Third-Order Nanocircuit Elements for Neuromorphic Engineering. *Nature* **2020,** *585* (7826), 518-23.

Table of Content

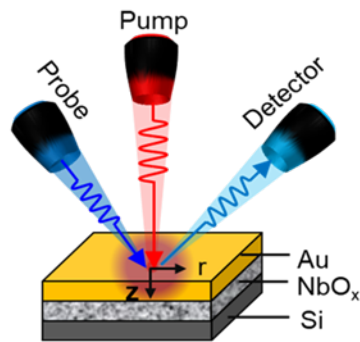

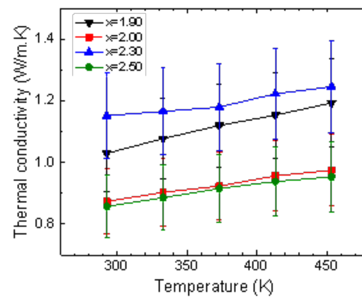

Supporting Information

Thermal conductivity of amorphous NbO_x thin-films and its effect on volatile memristive switching

Sanjoy Kumar Nandi[a], Sujan Kumar Das[a,b], Yubo Cui[c] Assaad El Helou[c], Shimul Kanti Nath[a,d], Thomas Ratcliff[a], Peter Raad[c] and Robert G. Elliman[a]*

[a] Department of Materials Physics, Research School of Physics, Australian National University, Canberra, Australian Capital Territory, 2601, Australia

[b] Department of Physics, Jahangirnagar University, Dhaka,1342, Bangladesh

[c] Mechanical Engineering Department, Southern Methodist University, Dallas, Texas 75275, United

States

[d] Department of Electrical, Electronic and Computer Engineering, The University of Western Australia, Crawley, Western Australia, 6009, Australia

E-mail: sanjoy.nandi@anu.edu.au

1. Thin film characterization

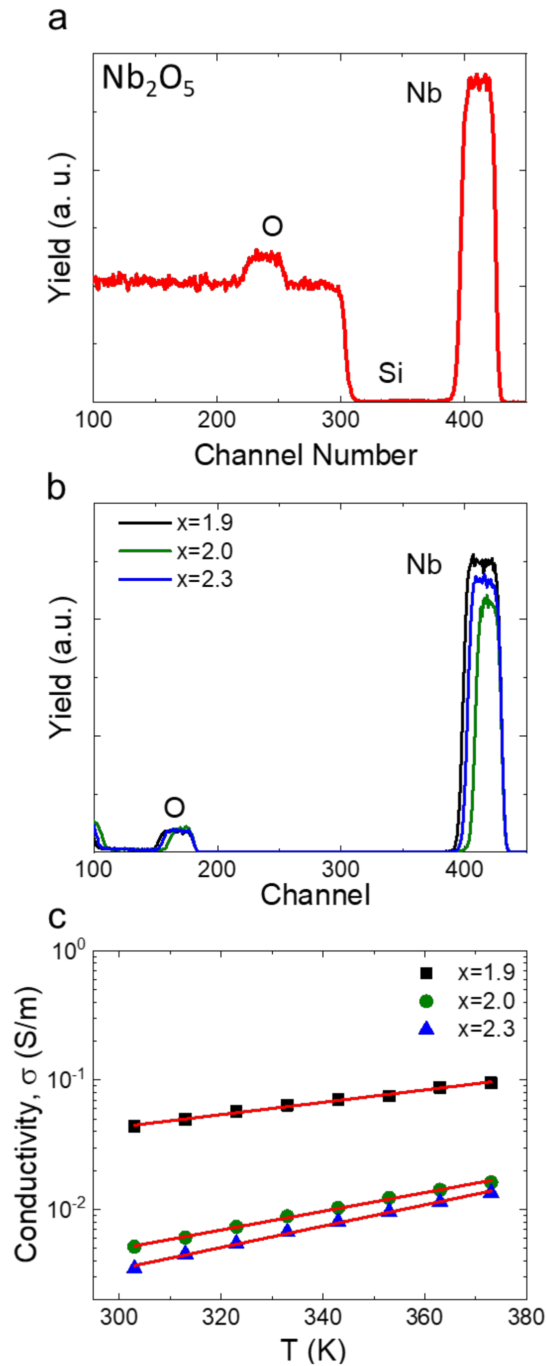

Figure S1: *Composition and conductivity data. (a) RBS spectrum of an Nb_2O_5 film on a Si substrate. (b) RBS spectra of substoichiometric NbO_x films deposited on vitreous carbon substrates. (c) Temperature-dependent two-terminal conductivity as a function of the stoichiometry of NbO_x.*

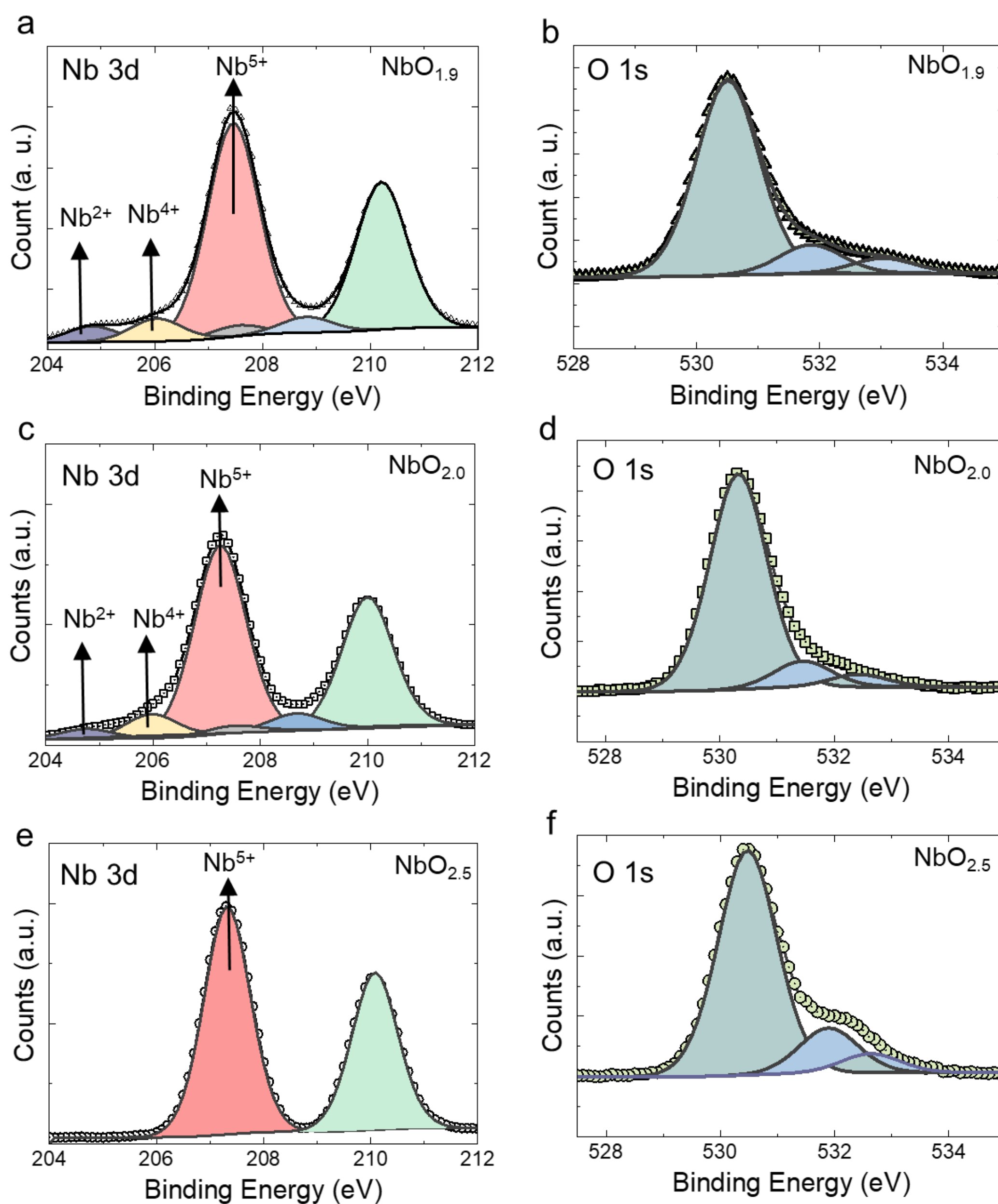

Figure S2. *X-ray photoelectron spectra (XPS): Nb3d and O1s core level spectra from (a-b) $NbO_{1.9}$ (c-d) $NbO_{2.0}$ and (e-f) $NbO_{2.5}$ films.*

The XPS spectra shown in Figure S2 were obtained from three different stoichiometric films. Two major peaks (207 eV and 209 eV) were observed in the Nb 3d core level spectra of the stoichiometric NbO_x (x=2.5) film. In contrast, the XPS spectra from substoichiometric NbO_x (x=1.9 and 2.0) showed contributions from both Nb^{2+}, Nb^{4+} and Nb^{5+}. [1]

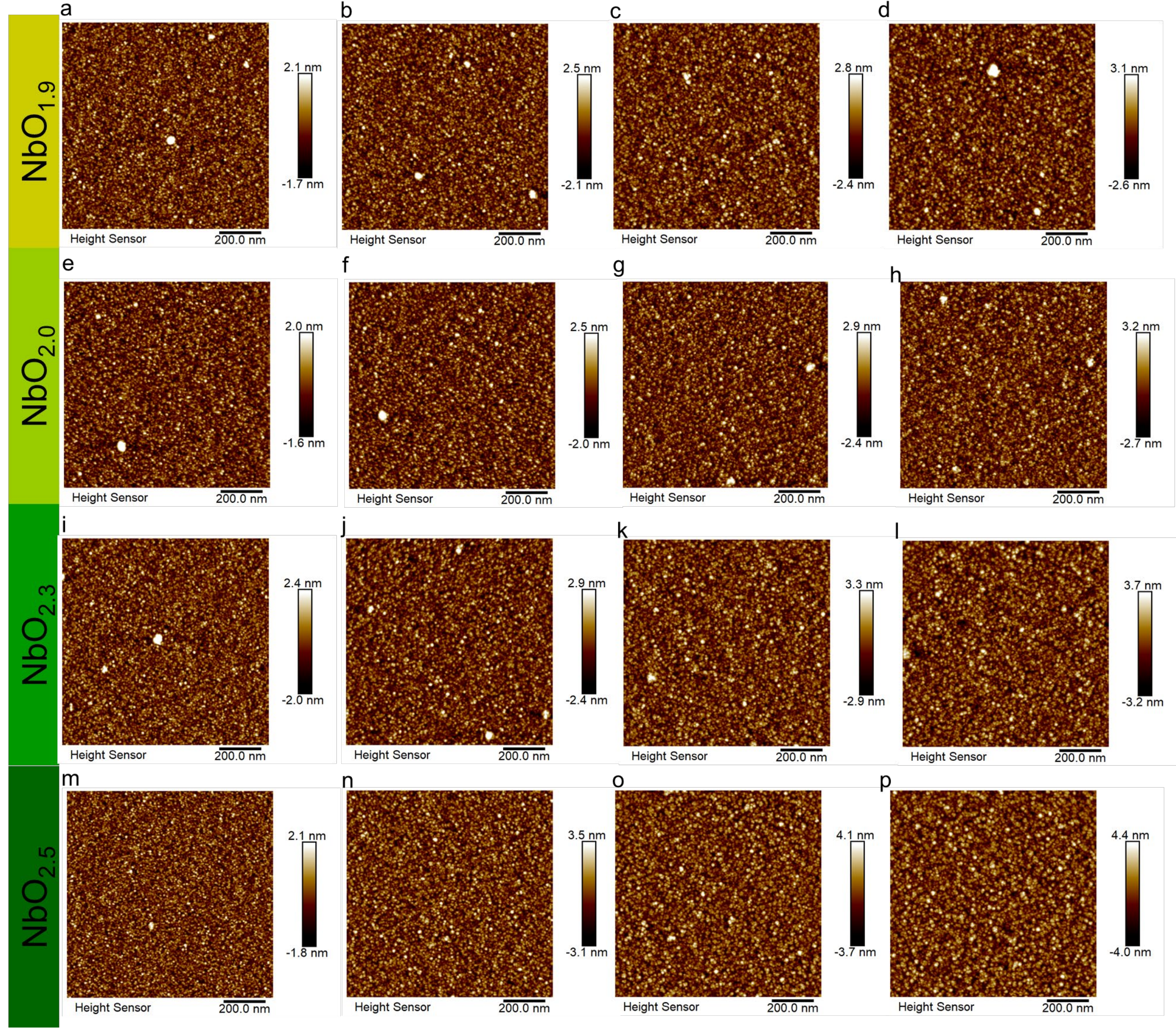

***Figure S3**: Surface roughness measurement of NbO_x thin films in the nanometer scale can be accurately determined using the atomic force microscopy (AFM). 2D surface topography of NbO_x films for different stoichiometric films: (a-d) $NbO_{1.9}$ films, (e-h) $NbO_{2.0}$ films, (i-l) $NbO_{2.3}$ films and (m-p) $NbO_{2.5}$ films.*

2. Calculation of minimum thermal conductivity

The minimum thermal conductivity was calculated using the models of Cahill *et al* [2] and Agne *et al* [3], according to the following formulae:

a) The minimum thermal conductivity of Cahill

The minimum thermal conductivity in this case is represented by a sum of three Debye integrals, where the sum is taken over the three sound modes (two translational and one longitudinal), with speeds v_i.

$$\mathrm{k}_{min}(T) \approx \left(\frac{\pi}{6}\right)^{\frac{1}{3}} k_B n^{\frac{2}{3}} \sum_i v_i \left(\frac{T}{\Theta_i}\right)^2 \int_0^{\frac{\Theta_i}{T}} \frac{x^3 e^x}{(e^x-1)^2} dx \qquad \text{(S1)}$$

The corresponding cutoff frequency for each polarization is given in degrees K by:

$$\Theta_i = \nu_i(\hbar/k_B)(6\pi^2 n)^{\frac{1}{3}} \quad \text{(S2)}$$

where n is the atomic density and T is the temperature.

Calculations were undertaken using the parameters listed in Table S1, where the transverse and longitudinal speeds of sound are taken from Mitterhuber *et al* [4].

b) The minimum thermal conductivity of Agne

The minimum thermal conductivity in this case is represented by the semiempirical equation:

$$\mathrm{k}_{min}(T) \approx \frac{n^{-\frac{2}{3}} k_B}{2\pi^3 \nu_S^3}\left(\frac{k_B T}{\hbar}\right)^4 \int_0^{0.95\frac{\Theta_D}{T}} \frac{x^5 e^x}{(e^x-1)^2}\,dx \quad \text{(S3)}$$

where the Debye temperature, Θ_D, is given by

$$\Theta_D = \frac{\hbar}{k_B}(6\pi^2 n)^{\frac{1}{3}}\nu_S \quad \text{(S4)}$$

and the speed of sound, ν_S, is taken as:

$$\nu_S = \frac{1}{3}(2\nu_T + \nu_L) \quad \text{(S5)}$$

where ν_T is the transverse sound velocity and ν_L is the longitudinal sound velocity, and as above, n is the atomic density and T is the temperature.

Calculations were undertaken using the parameters listed in Table S1. We note that the speed of sound for this case was taken from Cheng *et al.*[5]

Table S1*: Parameters used for calculating the minimum thermal conductivity.*

	Cahill	**Agne**
Atomic Density	6.82x10^{28} atoms.m^{-3}	6.82x10^{28} atoms.m^{-3}
Longitudinal sound velocity (ν_L)	5311 ms^{-1}	5311 ms^{-1}
Transverse sound velocities (ν_T)	3202 ms^{-1}	3202 ms^{-1}
Speed of sound (ν_S)		5000ms^{-1}

3. LT Spice modelling

The static and dynamic electrical response of devices were simulated using a previously reported lumped element thermal model[6], where the temperature dependent electrical conductivity of the NbOx film was assumed to be governed by the Poole-Frenkel mechanism, such that the device resistance is given by:

$$R = R_0 e^{(E_a + \beta\sqrt{E})/k_B T} \quad \text{(S6)}$$

$$\beta = \sqrt{\frac{e^3}{\pi\epsilon_0\epsilon_r}} \quad \text{(S7)}$$

This model is based on Newton's law of cooling:

$$\frac{dT}{dt} = \frac{1}{C_{th}}\left[RI^2 - \frac{1}{R_{th}}(T - T_{amb})\right] \quad \text{(S8)}$$

where C_{th} is the thermal capacitance and R_{th} is the thermal resistance of the active volume. Transposing gives:

$$RI^2 = C_{th}\frac{dT}{dt} + \frac{1}{R_{th}}(T - T_{amb}) \quad \text{(S9)}$$

which is represented by the equivalent circuit model shown in Figure S4, where the source current is set to the Joule heating power RI_s^2, and the voltage at point T represents the temperature, T.

In the present study, we explore the effect of variations in the magnitude and temperature dependence of R_{th}that reflect the measured changes. This is achieved by setting the thermal resistance to:

$$R_{th} = R_{th0}/(1 + \alpha(T - T_{amb}) \quad \text{(S10)}$$

With R_{th0} varying between 1.7x10^5 and 1.3x10^5 K/W and α set to 0 or 6x10^{-4} K^{-1} for temperature independent and temperature dependent thermal conductivity, respectively. (NB: These values were chosen to represent changes observed experimentally).

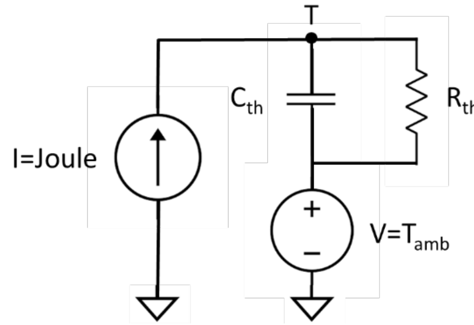

***Figure S4**: Lumped element circuit model of the Memristor.*

The quasi-static and oscillator-dynamics of devices were studied by simulating the response of the circuits shown in Figure S5 using LT-Spice, and the parameters employed for these studies are listed in Table S1. (NB: For comparison, key parameters are taken from Slesazeck *et al.*[6])

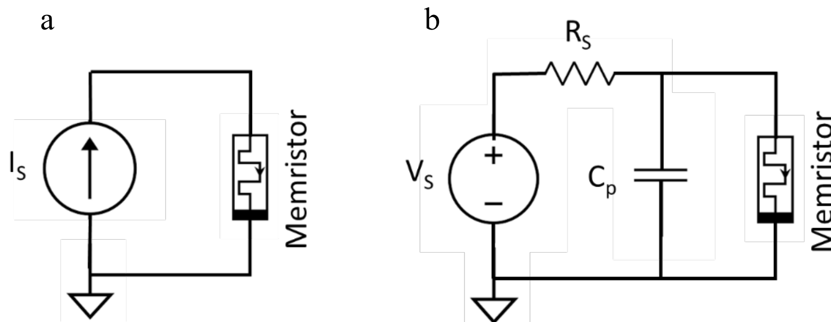

Figure S5: *(a) Quasi-static circuit; (b) Oscillator-circuit*

Table S2: *The parameters used in quasi-static and oscillator dynamics simulations*

Parameter	Value	Units
R_0 (film)	65	[Ω]
E_a	0.215	$[eV]$
ϵ_r	45	
R_{th0}	1.3×10^5 *to* 1.7×10^5	[K/W]
C_{th}	2.5×10^{-13}	$[J/K]$
α	0, $6x10^{-4}$	$[K^{-1}]$
T_{amb}	298	$[K]$
V_s	0 to 10	$[V]$
R_s	100-1500	[Ω]
C_p	10^{-8}	$[F]$

4. Finite element modelling (COMSOL)

Finite element modelling was undertaken using COMSOL v6.0 with the metal-oxide-metal device structure defined using the 2D axisymmetric model shown in Figure S6.

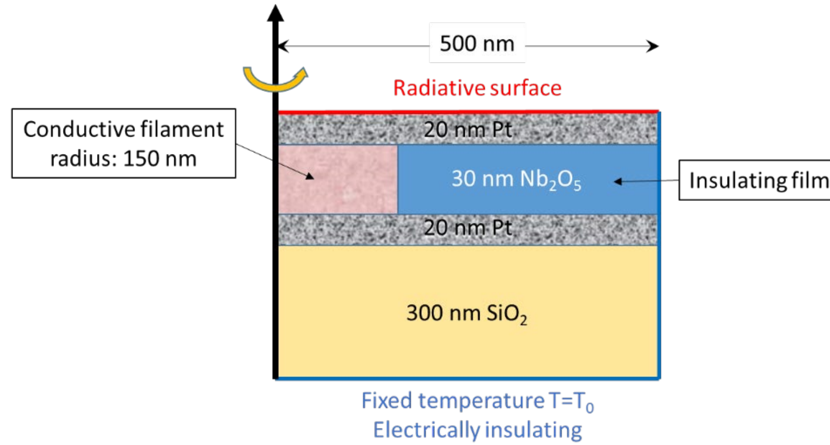

Figure S6: *Schematic of axisymmetric model employed for finite element modelling. Also included are the relevant boundary conditions.*

Calculations were performed for a current source applied to top Pt electrode with bottom Pt electrode grounded. The current and heat transport equations were solved using material data for Pt, SiO_2 and NbO_x from COMSOL library but with the electrical and thermal conductivity of the Nb_2O_5 film given by:

$$\sigma = \sigma_0 e^{(-E_a + \beta\sqrt{E})/k_B T} \tag{S11}$$

with

$$\beta = \sqrt{\frac{e^3}{\pi \epsilon_0 \epsilon_r}} \tag{S12}$$

$$\kappa_{th} = k_{tho}(1 + \alpha(T - T_0)) \qquad \text{(S13)}$$

using the parameters listed in Table. S3:

Table S3: *The parameters used in quasi-static and oscillator dynamics simulations*

Parameter	Value	Units
σ_0 (filament)	6.5×10^3	$[S.m^{-1}]$
σ_0 (film)	10	$[S.m^{-1}]$
E_a	0.215	$[eV]$
κ_{th0}	0.8, 1.0, 1.2	$[WK^{-1}m^{-1}]$
α	0, $6\text{x}10^{-4}$	$[K^{-1}]$
ϵ_r	45	
T_0	298	$[K]$

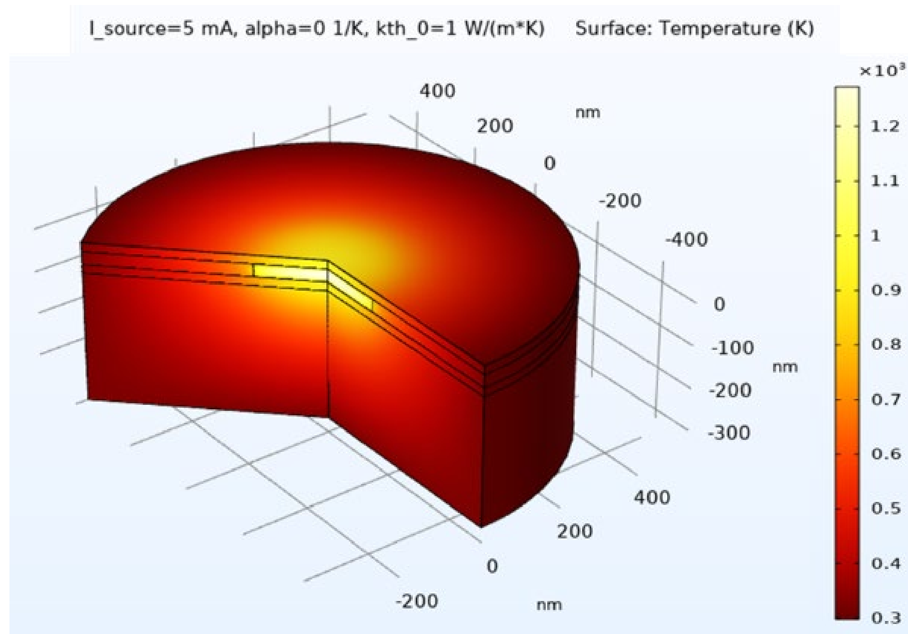

Figure S7: *Simulated temperature distribution in device for a current of 5 mA. Simulation parameters* α*=0* K^{-1}*,* k_{th}*=1* $WK^{-1}m^{-1}$*.*

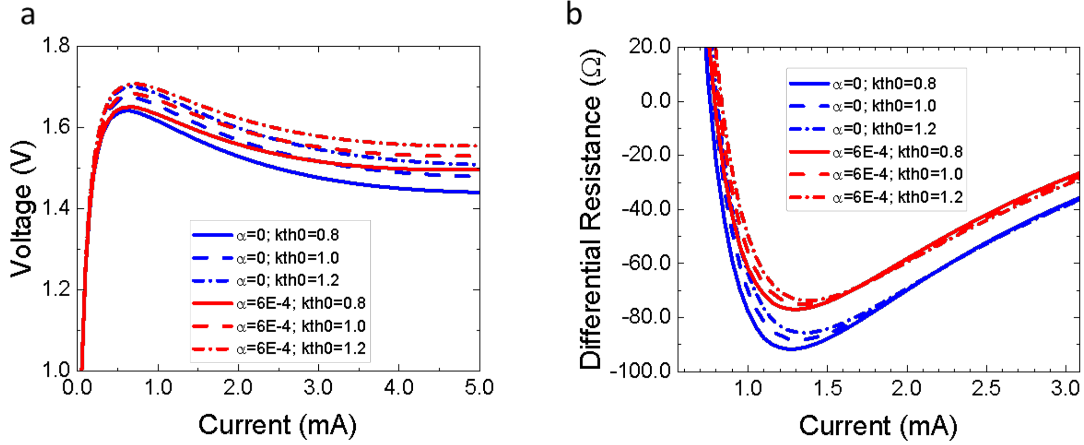

Figure S8: *Calculated (a) I-V characteristics and (b) differential resistance as a function of* α *and* k_{th0}.

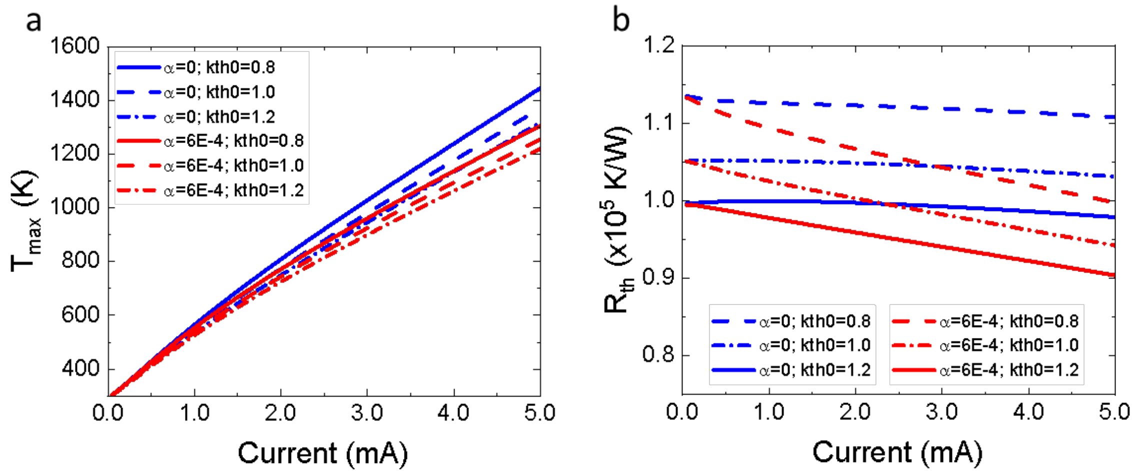

Figure S9: *(a) Maximum filament temperature and (b)* R_{th} *calculated from COMSOL simulation. NB:* R_{th} *was calculated using a lumped element approximation:* $T=T_0+R_{th}IV$*, where T was taken as the average filament temperature,* $T_0=298$ *K, I is the device current and V is the device voltage.*

5. Stoichiometric dependent of current-voltage characteristics

Preforming IV characteristics of substoichiometric NbO_x (x=1.9, 2.0 and 2.3) memristors as a function temperature are shown in Figure S9. It is important to note here that for the voltage sweep range (-0.5 V ↔ 0 ↔ +0.5 V) no current is observed for stoichiometric NbO_x (x=2.5) thin films as films are highly insulating.

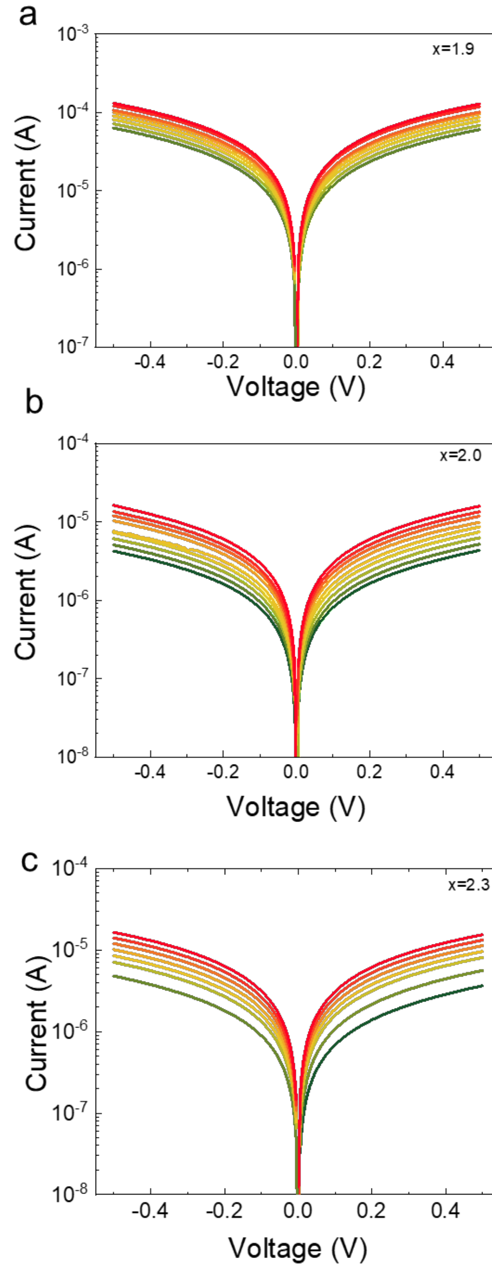

***Figure S10**: Preforming current-voltage (I-V) characteristics of (a) $NbO_{1.9}$ (b) $NbO_{2.0}$ and (c) $NbO_{2.3}$ thin film based Pt/Nb/NbO_x/Pt memristors. .*

We have previously reported electrical behaviour of NbO_x cross-point devices as a function of stoichiometry of NbO_x[7-8]. S-type characteristics of different stoichiometric NbO_x films are shown in Figure S11a-d. We further showed that the switching nature (modes, threshold voltage) is area and thickness independent in stoichiometric NbO_x(x=2.5) as the switching region considered to be localized near the interface[9]. However, in stoichiometric films the switching (modes, threshold voltage) is both thickness and area dependent as shown in Figure S11e-f [7-8]. Because the electrical conductivity of NbO_x films is a strong function of stoichiometry (Figure S1b). Therefore, it is difficult to draw conclusion about the role of the thermal conductivity from such measurements.

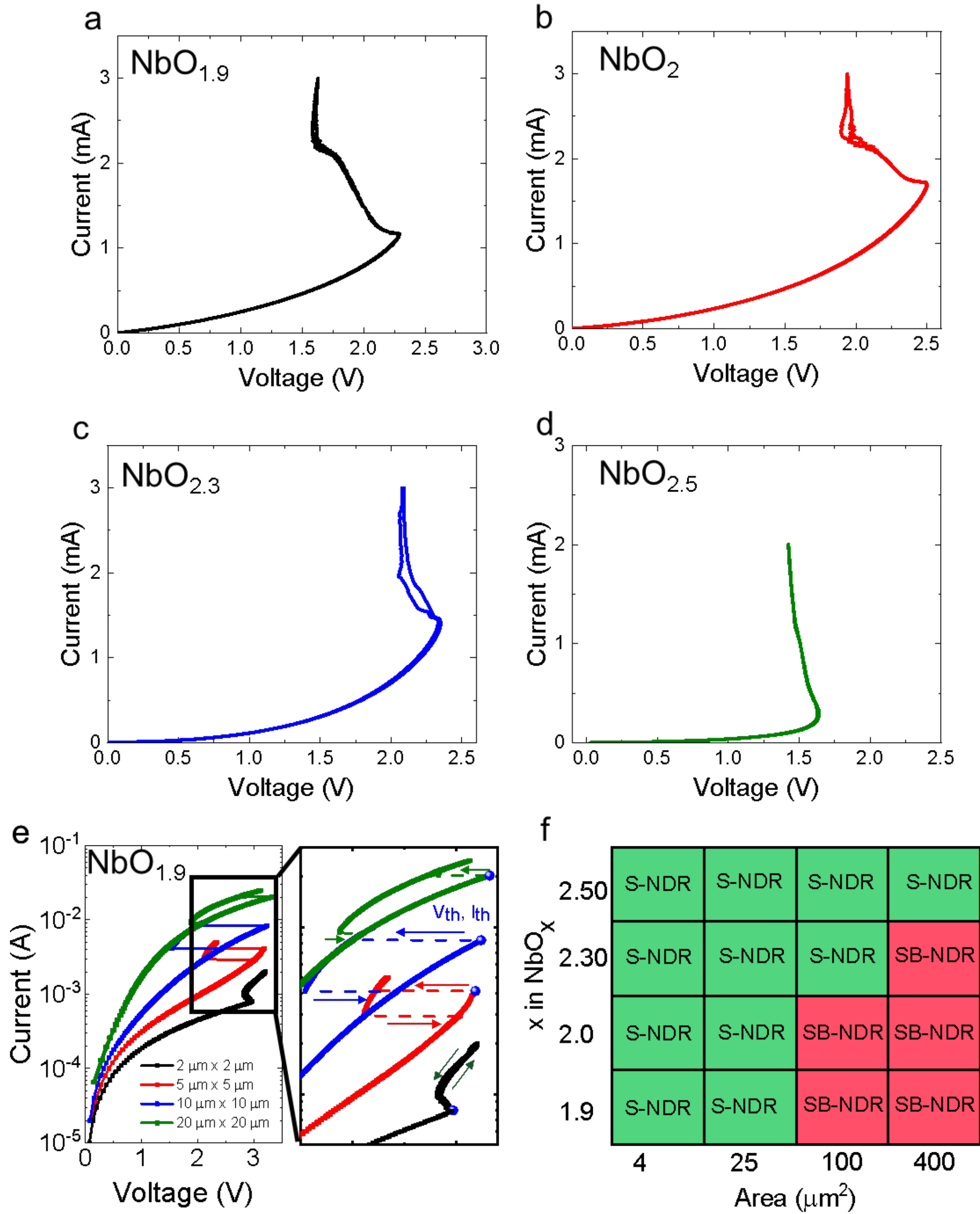

Figure S11: *S-type NDR characteristics of (a) Pt/Nb/$NbO_{1.9}$/Pt (b) Pt/Nb/NbO_2/Pt (c) Pt/Nb/$NbO_{2.3}$/Pt (c) Pt/Nb/$NbO_{2.5}$/Pt cross-point devices (5μ x 5μ). (d) Area dependent NDR characteristics in (e) Pt/Nb/$NbO_{1.9}$/Pt devices. (f) A summary of NDR modes as function of device size and stoichiometry.*

References:

1. Nath, S. K.; Nandi, S. K.; Ratcliff, T.; Elliman, R. G., Engineering the Threshold Switching Response of Nb2o5-Based Memristors by Ti Doping. *ACS Applied Materials & Interfaces* **2021,** *13* (2), 2845-52.
2. Cahill, D. G.; Watson, S. K.; Pohl, R. O., Lower Limit to the Thermal Conductivity of Disordered Crystals. *Phys Rev B Condens Matter* **1992,** *46* (10), 6131-40.
3. Agne, M. T.; Hanus, R.; Snyder, G. J., Minimum Thermal Conductivity in the Context of Diffuson-Mediated Thermal Transport. *Energy & Environmental Science* **2018,** *11* (3), 609-16.
4. Mitterhuber, L.; Kraker, E.; Defregger, S., Structure Function Analysis of Temperature-Dependent Thermal Properties of Nm-Thin Nb2o5. *Energies* **2019,** *12* (4).
5. Cheng, Z.; Weidenbach, A.; Feng, T.; Tellekamp, M. B.; Howard, S.; Wahila, M. J.; Zivasatienraj, B.; Foley, B.; Pantelides, S. T.; Piper, L. F. J.; Doolittle, W.; Graham, S., Diffuson-Driven Ultralow Thermal Conductivity in Amorphous Nb2o5 Thin Films. *Physical Review Materials* **2019,** *3* (2), 025002.
6. Slesazeck, S.; Mähne, H.; Wylezich, H.; Wachowiak, A.; Radhakrishnan, J.; Ascoli, A.; Tetzlaff, R.; Mikolajick, T., Physical Model of Threshold Switching in Nbo 2 Based Memristors. *RSC Adv.* **2015,** *5* (124), 102318-22.
7. Nandi, S. K.; Nath, S. K.; El-Helou, A. E.; Li, S.; Liu, X.; Raad, P. E.; Elliman, R. G., Current Localization and Redistribution as the Basis of Discontinuous Current Controlled Negative Differential Resistance in Nbox. *Adv. Funct. Mater.* **2019,** *29* (50), 1906731.
8. Nath, S. K.; Nandi, S. K.; El-Helou, A.; Liu, X.; Li, S.; Ratcliff, T.; Raad, P. E.; Elliman, R. G., Schottky-Barrier-Induced Asymmetry in the Negative-Differential-Resistance Response of $\Mathrm{Nb}/{\Mathrm{Nb}\Mathrm{O}}_{X}$/$\Mathrm{Pt}$ Cross-Point Devices. *Physical Review Applied* **2020,** *13* (6), 064024.
9. Shuai, L.; Xinjun, L.; Sanjoy Kumar, N.; Robert Glen, E., Anatomy of Filamentary Threshold Switching in Amorphous Niobium Oxide. *Nanotechnology* **2018,** *29* (37), 375705.